East African Journal of Engineering
eaje.eanso.org
Volume 7, Issue 1, 2024
Print ISSN: 2707-5389 | Online ISSN: 2707-5397
Title DOI: https://doi.org/10.37284/2707-5397
EAST AFRICAN NATURE & SCIENCE ORGANIZATION

Original Article

Ultra Enhancement of the Resolution of the Divergence Beam-Based SPR Sensor Using a Wavelet Filter

Jordan H. Hossea[1*]

[1] Dar es Salaam Institute of Technology, P. O. Box 2958 Dar-es-salaam, Tanzania.
* Author for Correspondence Email: jordan.hossea@dit.ac.tz

Article DOI : https://doi.org/10.37284/eaje.7.1.2365

Publication Date:

03 November 2024

Keywords:

Wavelet filter, SPR Sensor, Divergence Beam, Resolution, Combined Sensitivity Factor (CSF)

ABSTRACT

Surface Plasmon Resonance (SPR) sensors are highly sensitive to refractive index variations, making them ideal for biosensing and chemical detection applications. However, their performance can be constrained by noise, resolution limits, and signal distortions, particularly in divergence beam-based configurations. This research presents an ultra-enhancement of the performance of divergence beam-based SPR sensors by employing advanced wavelet filtering techniques. Wavelets, with their multi-resolution analysis capability, are applied to denoise and refine the sensor signal, significantly improving key performance metrics, including resolution, mean square error (MSE), root mean square error (RMSE), signal-to-noise ratio (SNR), sensitivity matrix (SM), and combined sensitivity factor (CSF).The wavelet filter effectively decomposes the SPR signal into distinct frequency bands, separating noise while retaining high-frequency components required for accurate sensing. This results in a significant reduction in MSE and RMSE of 30 and 92.26%, respectively, while simultaneously improving SNR by 54.08%, maintaining signal quality. The wavelet filter significantly improved the resolution of the SPR sensor by 99.95% (1.3772×10^{-7} RIU), allowing for more precise detection of refractive index changes and boosting diverge beam-based SPR sensor performance. In addition, a sensitivity matrix (SM) and combined sensitivity factor (CSF) were improved by 42 and 41.94%, respectively, allowing for a more thorough evaluation of the sensor's performance across multiple operational parameters. Simulation and experimentation show that wavelet filtering surpasses standard filtering approaches in terms of noise suppression and signal clarity. This technology has considerable potential for improving the accuracy and reliability of SPR sensors in high-sensitivity applications.

APA CITATION

Hossea, J. H. (2024). Ultra Enhancement of the Resolution of the Divergence Beam-Based SPR Sensor Using a Wavelet Filter. *East African Journal of Engineering*, 7(1), 283-301. https://doi.org/10.37284/eaje.7.1.2365

CHICAGO CITATION

Hossea, Jordan H. 2024. "Ultra Enhancement of the Resolution of the Divergence Beam-Based SPR Sensor Using a Wavelet Filter". *East African Journal of Engineering* 7 (1), 283-301. https://doi.org/10.37284/eaje.7.1.2365.

HARVARD CITATION

Hossea, J. H. (2024) "Ultra Enhancement of the Resolution of the Divergence Beam-Based SPR Sensor Using a Wavelet Filter", *East African Journal of Engineering*, 7(1), pp. 283-301. doi: 10.37284/eaje.7.1.2365.

Article DOI: https://doi.org/10.37284/eaje.7.1.2365

IEEE CITATION

J. H., Hossea "Ultra Enhancement of the Resolution of the Divergence Beam-Based SPR Sensor Using a Wavelet Filter" *EAJE*, vol. 7, no. 1, pp 283-301, Nov. 2024.

MLA CITATION

Hossea, Jordan H "Ultra Enhancement of the Resolution of the Divergence Beam-Based SPR Sensor Using a Wavelet Filter" *East African Journal of Engineering*, Vol. 7, no. 1, Nov. 2024, pp. 283-301, doi:10.37284/eaje.7.1.2365.

INTRODUCTION

The oscillation of the surface charge at the gold/sample interface with a certain frequency is called surface plasmon (SP) [1]. The SP generates surface plasmon waves (SPW) at the gold-sample interface. The oscillation frequency of the SP depends on the refractive index of the sample. At an angle of incidence greater than the critical angle, the evanescent wave is generated, which tends to interact with the plasmon wave. As the incidence increases beyond the critical angle, total internal reflection disappears, which is called attenuated total internal reflection (Kretschmann, 1971; Otto, 1968). This implies that the evanescent wave and the surface plasmon wave are resonant. The angle of incidence at which the resonance occurred is called the resonance angle at which the surface plasmon resonance (SPR) effect occurs. The SPR angle varies depending on the change in the refractive index (RI) of the sample (Kretschmann & Raether, 1968). That is, the higher the RI, the higher the SPR angle.

The SPR angle varies depending on the change in the refractive index (RI) of the sample, meaning that the higher the RI, the higher the SPR angle. Therefore, the measurement of the SPR sensor depends on the condition of the sensor medium. The reflected signal is captured by the CCD/CMOS sensor. The absorbed part of the signal is indicated by the dark band.

The SPR sensor have numerous merits such as evasive measurement, requires small sample. Besides of good performance of the SPR sensor in comparison to others optical sensor. The reported work shows that angular interrogation SPR based sensor gives high sensor sensitivity and resolution. Angular interrogation is implemented by scanning the incidence beam by varying the angle. There are three mechanisms of the implementing the angular scanning namely, mechanical, converging and diverging beam scanning (Boruah, Mohanta, Choudhury, Nath, & Ahmed, 2015; Chen et al., 2015; Huang et al., 2020; Mohanty & Kasiviswanathan, 2005). The mechanical scanning beam measure the samples with wide range of change of refractive index because it involves mechanical rotation of either the laser beam or sensing stage (Pluchery, Vayron, & Van, 2011). However, due the mechanical rotation the system is prone to noise such as thermal noise and displacement shift (Boruah et al., 2015; Huang et al., 2020; Mohanty & Kasiviswanathan, 2005). Meanwhile, converging beam scanning gives improved sensitivity because of absence of the mechanical scanning, but it is limited to narrow range which can be limited to the application which requires wide range of the sample measurements (Hickel & Knoll, 1991; Lenferink, Kooyman, & Greve, 1991; T. Wang, Zhang, Aleksov, Salama, & Kar, 2016).

Diverging beam scanning obviates the effect of the mechanical rotation and measures wide range of the sample without mechanical scanning (Hu et al., 2016; Karabchevsky, Karabchevsky, & Abdulhalim, 2011). Researchers have implemented divergence beams by using the cylindrical lens (J. Hossea & WidJaJa, 2020; Hu et al., 2016; Karabchevsky et al., 2011). However, the cylindrical lens can diverge the beam in narrow range which makes it unsuitable for wide range of measurement (Chan & Jutamulia, 2012; Chinowsky, Quinn, Bartholomew, Kaiser, & Elkind, 2003; Isaacs & Abdulhalim, 2015). Additionally, a cylindrical lens produces Gaussian beam distribution in which the beam appears bright at the center and dark at their edge, which requires complex mathematical algorithm in the detecting minimum dip (Chan & Jutamulia, 2012; Chen et al., 2015; Isaacs & Abdulhalim, 2015). Thus, to cover wide range of the sample

Article DOI: https://doi.org/10.37284/eaje.7.1.2365

measurement the SPR sensor requires an optical component which diverges the beam uniformly and with higher fan angle such as Powell lens (J. H. Hossea & Widjaja, 2017; Widjaja & Hossea, 2021). The widening of the diverged beam depends on the fan angle of the Powell lens and the location of the CCD/CMOS imaging sensor (J. H. Hossea & Widjaja, 2017; Widjaja & Hossea, 2021).

Because of the considerable separation distance between the Powell lens and the image sensor, the divergent beam size is estimated to increase from 3 to 5 cm, thus the beam appears larger at the exiting side of the prism (J. H. Hossea & Widjaja, 2017; Widjaja & Hossea, 2021). As results of bigger size which can easily be corrupted by dust particles or any other presence mark/scratches or dust particle on the prism surface. Birefringence effect occurred in the prism leads to laser source to be in out of focus, variation in polarization which results wrong resonance position (Ohkita, Abe, Kojima, Tagaya, & Koike, 2004), hence false detection. Again laser source is prone to speckle noise (Goodman, 2007). Consequently, the reflected beam seems to be big, the reflected signal captured by the CMOS/CCD sensor can easily be contaminated by stain and shading, scratches, spurious noise, resulting in a shallow minimum dip due to the background noise as it has been reported (de Aguiar, Souza, de Souza, & Oliveira, 2022). Furthermore, it is difficult and costly to get the CCD/CMOS sensor that can collect the entire beam without positioning the observation plane. Meanwhile the observation plane can be a temporary solution of being able to capture an image with larger size than the image sensor size. Resulting reflected signal interacted with morphological structure of an observation plane can interact with the reflected signal as it translucent through it. Therefore, the combined interference effects from the prism surface are caused by both broad coverage and observation plane noise, often known as background noise. Furthermore, the SPR sensing mechanism is extremely sensitive to even little displacements or changes in the optical or observation plane (Moreira, Lima, Neff, & Thirstrup, 2008).

These background noises lead to false detection (incorrect location resonance position), shallow minimum dip, and deformation of the captured image as the result of plane of observation. The compound effect is the reduction of the SPR sensor's sensitivity, detection accuracy, and resolution (Oliveira, Lima, Thirstrup, & Neff, 2019).

Much research was conducted on reducing or minimizing noise effect (Boecker, Zybin, Niemax, Grunwald, & Mirsky, 2008; Patskovsky, Meunier, Prasad, & Kabashin, 2010). Speckle noise is a type of noise that oscillates at high frequencies, hence a low pass filter is excellent choice for removing it (Pavlov, Vedyashkina, & Yanina, 2019). Another filter is the average filter, which takes the mean of selected rows or columns in a picture and faces the difficulty of removing background noise (Pavlov et al., 2019). Meanwhile, other filters are appropriate for treating only laser source variation and shot noise. A Gaussian filter was developed for postprocessing, with full width half maximum (FWHM) and resonance angle as parameters (G. Wang, Wang, Ren, Ma, & Li, 2022). The two parameters were utilized to model Gaussian expression. Despite being an effective strategy for improving the sensing capability of the SPR sensor, the filter will get difficult when numerous samples are detected at the same time (G. Wang et al., 2022).

The fundamental purpose of this research is to design the filter that eliminates background noise using the wavelets filter, which is capable of filtering noise with multiple samples simultaneously. Wavelet filters can improve signal-to-noise ratios and reproduce signals that are comparable to the original less distortion. As a result, the sensitivity, detection accuracy, and resolution of the SPR sensor can be improved without modifying its physical structure configuration. The contribution of this work is.

- To improve the minimum dip of the SPR sensor reflectivity by using Wavelet filter.

Article DOI: https://doi.org/10.37284/eaje.7.1.2365

- To apply wavelet filter to improve full width at half maximum (FWHM) by smoothing out unfiltered noise.
- To enhance detection accuracy due to reduction of the noise oscillation around the reflectivity curve.
- To improving SPR sensor resolution by optimizing the signal to noise ratio.

Methodology

SPR sensor using Powell lens.

The schematic diagram of divergent beam illumination based on SPR sensor setup using Powell lens is shown in **Fig. 1**. The configuration is based on Kretschmann (Kretschmann & Raether, 1968), in which the *p*-polarized beam of light is illuminated to excite SPR effects. Powell lens used to diverge evenly photon energy. This beam is incident at a particular angle on the side *AC* of a prism with an apex angle ϕ. To cover the sample with the range of refractive index from n_1 to n_2. The angles α_{i2} is the critical angle between prism-air interface while β_{i2} is the angle which is higher than the resonance angle of the maximum sample to be measured. In which transmitted rays *EG* and *FH* are which are incident at the prism–gold film which correspond to critical angle and resonance angle of the maximum measured sample, respectively (J. Hossea & WidJaJa, 2020; Widjaja & Hossea, 2021).

Figure 1. Schematic illustration of the divergent illumination based SPR sensor setup using Powell lens.

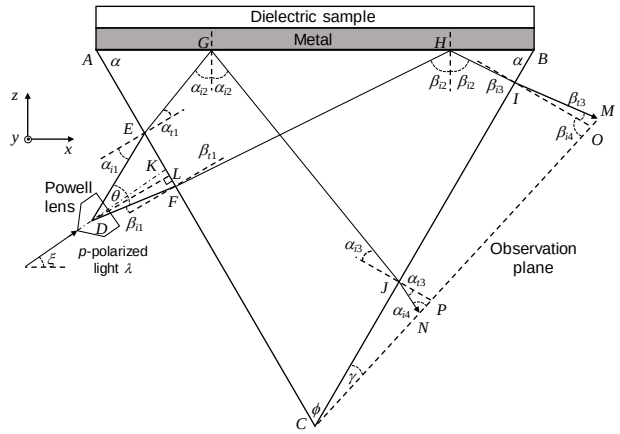

Derivation of the angle of inclination

The angles α_{i2} and β_{i2} are derived by using the Snell's law by considering the diverging beam at the side *AC* as(J. Hossea & WidJaJa, 2020; Widjaja & Hossea, 2021)

$$\alpha_{i1} = \arcsin\left[n_p \cos(\phi/2 + \alpha_{i2})\right] \quad (1)$$

and

$$\beta_{i1} = \arcsin\left[n_p \cos(\phi/2 + \beta_{i2})\right], \quad (2)$$

respectively. The formula for finding the fan angle is expressed as in Eq (3.3). It is an important parameter in identifying the suitable Powel lens to fit particular application(J. Hossea & WidJaJa, 2020; Widjaja & Hossea, 2021).

$$\theta = \alpha_{i1} - \beta_{i1}$$

$$\theta = \arcsin\left[n_p \cos(\varphi/2 + \alpha_{i2})\right] + \arcsin\left[n_p \cos(\varphi/2 + \beta_{i2})\right], \quad (3)$$

The angle for tilting the laser source is expressed as (Widjaja & Hossea, 2021).

Article DOI: https://doi.org/10.37284/eaje.7.1.2365

$$\xi = (\phi + \theta)/2 - \beta_{i1}$$

$$= (\phi + \theta)/2 + \arcsin\left[n_p \cos(\phi/2 + \beta_{i2})\right].$$

The angle is measured with reference of the *x* axis.

When the oscillation of the incident photon energy and surface charge at the gold-sample interface, the resonance angle is formed β_{spr} at the side *AC* and is expressed as (Kretschmann & Raether, 1968)

$$\beta_{spr} = \sin^{-1}\left(\frac{1}{n_p}\sqrt{\frac{n_m^2 n_s^2}{n_m^2 + n_s^2}}\right) \quad (5)$$

The totally reflected beam is captured through the observation plane which is inclined at γ with respect to the prism side *BC*. The observation plane was used, because the size of the beam was 3 cm which was not possible to take CMOS sensor at the time (J. Hossea & WidJaJa, 2020).

$$\gamma = (\alpha_{i1} + \beta_{i1})/2. \quad (6)$$

As a results of introducing the observation angle between side *BC* of the prism and detector, the researcher observed some noise that needs to filter to obtain clear signal to optimize the performance of the SPR sensor.

Derivation of the Beam widths

The width *EF* of the beam at side *AC* from the Powell lens is calculated by (J. Hossea & WidJaJa, 2020; Widjaja & Hossea, 2021)

$$EF = \frac{DL\sin\theta}{\cos\alpha_{i1}\cos\beta_{i1}} \quad (7)$$

with *DL* is the normal distance from the prism surface to the focal point of the lens.

By subtracting triangles ΔAGE and ΔAHF, the length of the beam *GH*, on the hypotenuse side of the prism is expressed as(J. Hossea & WidJaJa, 2020)

$$GH = \left\{ AE\left(\frac{\sin(\varphi/2 + \beta_{i2})}{\cos\beta_{i2}} - \frac{\sin(\varphi/2 + \alpha_{i2})}{\cos\alpha_{i2}}\right) + EF\left(\frac{\sin(\varphi/2 + \beta_{i2})}{\cos\beta_{i2}}\right)\right\} \quad (8)$$

Beam length *GH* is important for selecting the proper size of gold-coated sensing chip.

The size of the beam at the exit side (*IJ*) of the prism, is given (J. Hossea & WidJaJa, 2020)

$$IJ = AB\left(\frac{\cos\alpha_{i2}}{\sin(\varphi/2 + \alpha_{i2})} - \frac{\cos\beta_{i2}}{\sin(\varphi/2 + \beta_{i2})}\right) - AE\left(1 - \frac{\sin(\varphi/2 + \alpha_{i2})\cos\beta_{i2}}{\sin(\varphi/2 + \beta_{i2})\cos\alpha_{i2}}\right) + GH\left(\frac{\cos\beta_{i2}}{\sin(\varphi/2 + \beta_{i2})}\right) \quad (9)$$

The beam size shone on the observation plane is found using (J. Hossea & WidJaJa, 2020),

$$MN = \frac{IJ\cos\beta_{i1} + BI(\cos\alpha_{i1} - \cos\beta_{i1})}{\cos\gamma}. \quad (10)$$

Experimental setup

Figure 2 is the Powell lens-based SPR sensor**.** The He-Ne laser light operates at the wavelength λ = 632.8 nm which passes through polarizing beam splitter cube to give out the *p*-polarization beam. The rotating half-wave plate is used to optimize the *p*-polarization light. The experiment used SF11 equilateral prism (n_p = 1.785) with a side length of 50 mm. Eqs. (1) and (2) were applied in determining the coverage range of the sample which is from 34˚to 57˚To test the working of the SPR sensor pure water RI= 1.3317, pure ethanol RI = 1.356, and air RI = 1 as the test samples. Based on the minimum fan angle θ of the

Article DOI: https://doi.org/10.37284/eaje.7.1.2365

divergent beam was found to be 46˚. To diverge p-polarized light equally, a Powell lens with a fan angle of 60˚ was employed. The incident distance AE was adjusted to 7.1 mm, and the Powell lens distance DL was 8 mm. To conduct each SPR measurement, a 20 mm × 20 mm Au evaporated glass plate (Nano SPR, BA1000) with the refractive index n_m = 0.1726 + j3.4218 (Yamamoto, 2002) was placed on top of side *AB* of the prism. In the prevention of light loss, a matching liquid (Cargille series A) was applied to the space between the prism and the glass plate. The test samples were dropped at specific locations on the glass plate using a 10-microliter pipette (Glassco). The drop position was calculated by inserting the resonance angle of the respective liquid into Eq. (8). A 2D CMOS image sensor (Sony Exmor R IMX251) with 7952 × 5304 pixels and a 35.9 mm x 23.8 mm area was used to capture totally reflected intensity patterns (Widjaja & Hossea, 2021). As a result, unlike the typical scanning approach, SPR reflectivity from a wide variety of angles may be detected with a single recording.

Figure 2. Experimental setup for implementing the divergent illumination-based SPR sensor using Powell lens (Widjaja & Hossea, 2021).

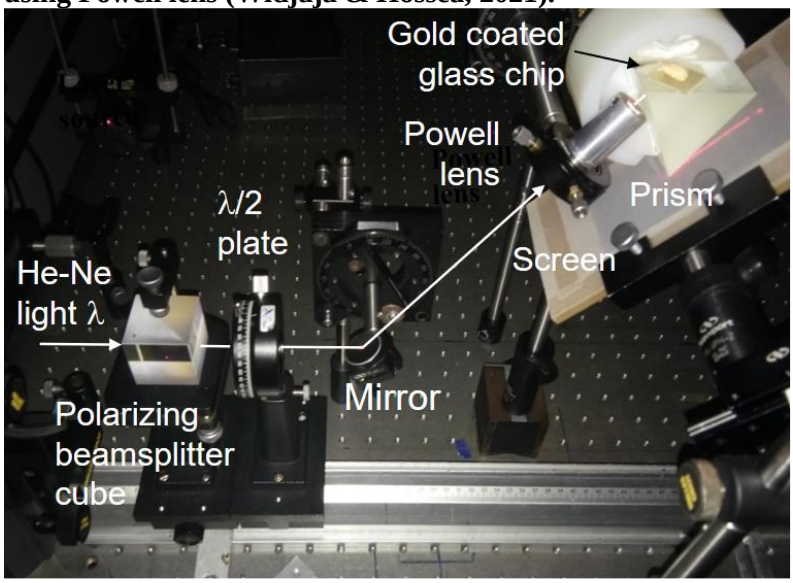

Noise level measurement for the filter

During the deployment of the filter and to evaluate the filter's effect on SPR sensor performance enhancement, the noise level must be quantified before and after application. To evaluate the noise level, the parameters mean square error (MSE), root mean square error (RMSE), and signal-to-noise ratio (SNR) were utilized.

a) **The mean square error (MSE)** quantifies the closeness of the wavelet filtered-SPR signal to the ideal SPR signal the smaller the value the better the filter performance (Balan, Khaparde, Tank, Rade, & Takalkar, 2014).

$$MSE = \frac{1}{N}\sum_{n=1}^{N}\left(R_i(n) - R_f^{'}(n)\right)^2 \quad (11)$$

b) **The root mean square error (RMSE)** which characterizes how close the filtered signal approaches the ideal SPR reflectivity. This signifies that the smaller the value the better the performance of the designed filter.

The RMSE is expressed as (Dai & Fu, 2024)

$$RMSE = \left(\frac{1}{N}\sum_{n=1}^{N}\left(R_i(n) - R_f^{'}(n)\right)^2\right)^{1/2} \quad (12)$$

Article DOI: https://doi.org/10.37284/eaje.7.1.2365

where N is the total number of CMOS pixels; $R_i(n)$ ideal SPR reflectivity without the effect of noise; and $R_f^{'}(n)$ is the wavelet filtered-SPR reflectivity.

c) **The signal-to-noise Ratio (SNR)** is the parameter that quantifies the capability of the filter to filter out noise and how the signal was distorted due to the application of the filter (Dai & Fu, 2024). Also, implies how the filtered signal has retained the ideal SPR reflectivity signal expressed (Dai & Fu, 2024)

$$SNR = 10\log_{10}\left(\frac{E_i}{E_n}\right)$$
$$E_i = \sum_{n=1}^{N}\left(R_i(n) - \overline{R_i(n)}\right)^2$$
$$E_n = \sum_{n=1}^{N}\left(R_i(n) - R_n^{'}(n)\right)^2 \quad (13)$$

where E_i is the SPR signal energy; E_n is the noise energy $R_i(n)$ ideal SPR reflectivity without being corrupted by noise, $\overline{R_i(n)}$ is the mean of the ideal SPR reflectivity and $R_n^{'}(n)$ is the SPR reflectivity after applying wavelet filter at different number of levels

Quantification of the SPR sensor performance

The SPR sensor measurement parameters were extracted from the resonance curve, in which sensitivity, detection accuracy, and quality factor. These performance parameters reveal how well the SPR biosensor functions.

a) Sensitivity (S)

The sensitivity of the SPR biosensor is measured as a change in resonance position in the reflectance curve ($\Delta\theta res$) corresponding to the small change in the refractive index (Δns) of the analyte (J. H. Hossea & Rugumira, 2024). The sensitivity(S) is given by,

$$S = \frac{\Delta\theta_{res}}{\Delta n_s} \quad (14)$$

b) Detection Accuracy (DA)

DA is inversely proportional to the full width at half maxima (FWHM) of the reflectance curve and is given by (J. H. Hossea & Rugumira, 2024),

$$DA = \frac{\Delta\theta_{SPR}}{FWHM}$$
$$DA = \frac{S\Delta n}{FWHM} \quad (15)$$

c) Quality Factor (QF)

The quality factor (*QF*) is given by, on the other hand, QF is defined as the ratio of S to the FWHM (J. H. Hossea & Rugumira, 2024), and has a unit of RIU^{-1}

$$QF = \frac{S}{FWHM}$$
$$QF = \frac{DA}{\Delta n} \quad (16)$$

d) Sensor merit

Sensor merit determines the narrowness of the SPR reflectivity curve and how photon energy is converted to plasmonic energy. The broadening of the SPR reflectance dip is evaluated by integrating the effect of sensor resolution and FWHM with the shape of resonance damping near the minimum. Thus, sensor merit is expressed as (Ceballos-Zumaya, Sustaita-Torres, Pérez-Huerta, Ariza-Flores, & Madrigal-Melchor, 2024; Sharma & Dominic, 2017; Vlcek, Pistora, & Lesnák, 2009)

$$SM = \frac{R_{\max} - R_{\min}}{FWHM} \quad (17)$$

e) Combined sensitivity factor

Article DOI: https://doi.org/10.37284/eaje.7.1.2365

Combined sensitivity factor (CSF), is the product of the sensitivity sensor merit (SM) in this work (Sharma & Dominic, 2017; Vlcek et al., 2009). Hence, the CSF is given by S multiplied by SM (Ceballos-Zumaya et al., 2024). The unit is RIU^{-1} and is stated as:

$$CSF = S \times SM \tag{18}$$

f) Resolution

Resolution is the parameter which the SPR sensor gives observable output to the smallest change in refractive index (Bahrami, Alam, Aitchison, & Mojahedi, 2013; Jiří Homola, 2008; Ma, Liu, Zhang, He, & Peng, 2019). Resolution depends on the standard deviation of the SPR sensor and the sensitivity of the sensor S

$$\sigma_s = \frac{K\sigma_{th}}{\sqrt{N}}\left(\frac{FWHM}{R_{\max} - R_{\min}}\right) \tag{19a}$$

$$\text{Resolution} = \frac{K\sigma_{th}}{S\sqrt{N}}\left(\frac{FWHM}{R_{\max} - R_{\min}}\right) \tag{19b}$$

$$\text{Resolution} = \frac{K\sigma_{th}}{\sqrt{N}}\left(\frac{1}{S \times SM}\right)$$

$$\text{Resolution} = \frac{K\sigma_{th}}{\sqrt{N}}\left(\frac{1}{CSF}\right) \tag{19c}$$

Where K is the combined factor of additive noise, shot noise, and noise due to light intensity fluctuation and is the standard deviation noise σ_{th} which is extracted from the vertical averaging of the reflected intensity captured by the CMOS sensor, in which $K\sigma_{th}$ is the equivalent standard deviation which comprises all noise effects. N is the total pixels of the CMOS sensor which covers from the minimum to the maximum range.

Results and Discussion

Effect of background SPR noise

Figure 3 (a) shows the image obtained by a CMOS sensor when the laser source's polarization is S. **Figure 3(b)** displays P-polarized with a faint minimum dip generated by the identification of air and water as samples which resulted from background noise. Meanwhile, **Figure 3(c)** displays P – polarized with a minimum dip of the air and ethanol samples. The minimal drop for air and water is plainly visible since the sample appears significantly darker than before background noise reduction. **Figure 3(b)** shows the two dark bands on the far left are the resonance position of the air sample while the far-right dark band is the resonance position of the water. Meanwhile **Figure 3(c)** the dark band situated on the far-left is for air while the dark band is located on the far-right side. This indicates that background noise affects the mechanism of assessing the minimum dip.

Figure 3 Experimental image captured by CMOS sensor for (a) S-polarized image (b) P-polarized image when the sample is air and water (b) P-polarized image when the sample is air and ethanol.

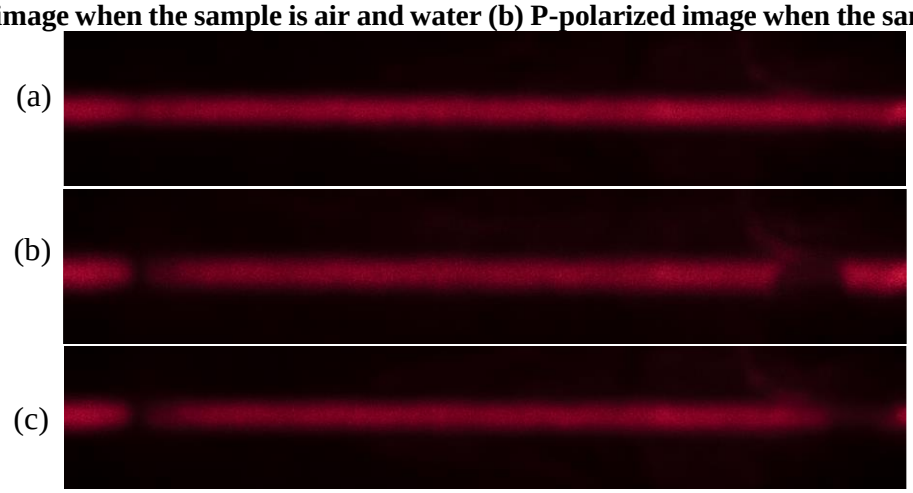

Article DOI: https://doi.org/10.37284/eaje.7.1.2365

The blind zone width refers to the phenomenon in the SPR sensor where multiple detections of a sample with marginally varying refractive indices are undetectable by any CMOS/CCD sensors, due to the thickening of the SPR reflectivity curve, leading to dark effects as illustrated in **Figure 3**. This effect is especially prominent in the divergence beam used to identify numerous samples with very similar refractive indices in a single shot, utilizing a CCD or CMOS sensor as a detector.

Figure 4 illustrates how the blind zone is estimated using the SPR reflection curve. **Figure 4** shows that the intended SPR sensor cannot detect minor variations in the refractive index closer to the air sample, with resonance angles ranging from 37.084 to 35.8235˚ or 37.6624 to 35.4705˚. A similar impact is observed when detecting materials whose RI is closer to water and whose resonance angle ranges between 55.7754 and 54.0107˚. The sensor cannot detect the transition clearly. For samples closer to ethanol, the resonance angle ranges from 57.5224 to 55.4966˚.

The second consequence is a reduction in the minimum dip, which is noticeable when the SPR reflectivity thickens and the minimum dip appears shallow. This can make it difficult to determine the minimal dip or need the employment of complicated algorithms (Karabchevsky et al., 2011). Because background noise has a significant influence, the visual assumption that the energy transfer efficiency drops to 54.336% is incorrect because the shallowness of the resonance position is caused by noisy SPR signals, not poor photon energy transfer.

Figure 4; **The noisy SPR reflectance**

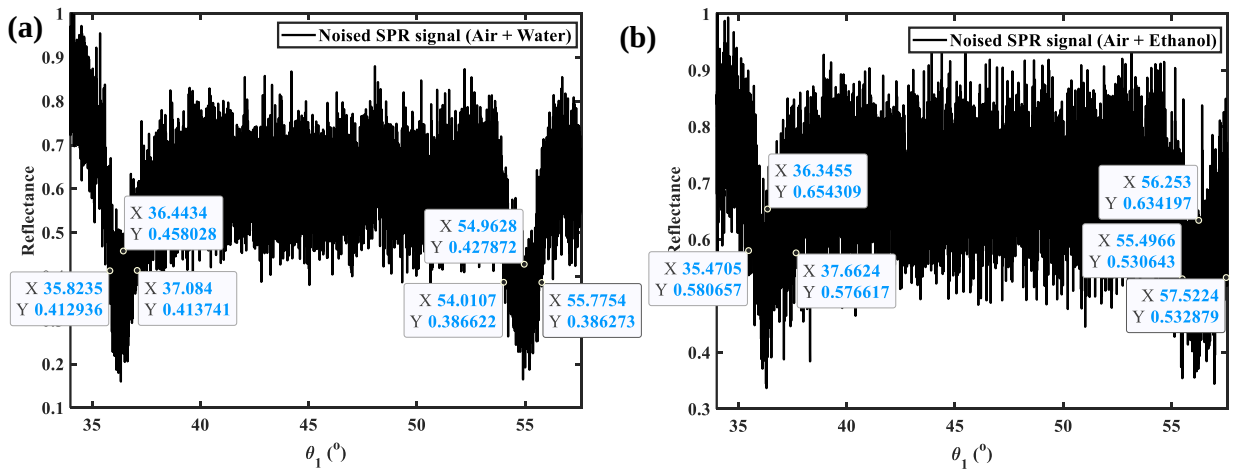

Design of Wavelet transform

Therefore, the purpose of this study is to design the wavelets filter which eliminates the effects of the background noise. The improve the detection accuracy and the resolution of the SPR sensor the proper SPR reflectivity curve enhancement must be adopted. DWT is the mathematical concept that decomposes the spatial domain into the frequency domain which is effectively applied in non-stationary signals. A function of $\psi(t) \in L^2(R)$ with zero basis can be defined as (Lee & Kim, 2015)

$$DWT(j,k) = \frac{1}{\sqrt{2^j}} \int_{-\infty}^{\infty} x(t) \psi^* \left(\frac{t - k2^j}{2^j} \right) \quad (20)$$

In eqn (17) consists of two parameters, which are translation factor k determines the oscillatory frequency, and dilation factor j signifies the length of the wavelet.

Consider using wavelet transform (DWT) for a function $f(t)$ with length of 2^N and J level is expressed as (Lee & Kim, 2015)

Article DOI: https://doi.org/10.37284/eaje.7.1.2365

$$f(t)=\sum_{k=0}^{2^{N-j}-1} a_{j,k}\phi_{j,k}(t)+\sum_{k=0}^{J} d_{j,k}\psi_{j,k}(t) \quad (21)$$

Where $a_{j,k}=\int f(t)\phi_{j,k}(t)dt$ is the scaling coefficient and $d_{j,k}=\int f(t)\psi_{j,k}(t)dt$ is the wavelet coefficient. Where J ($J \le N$) is the total number of decomposition levels while N is the maximum number of decomposition levels (Lee & Kim, 2015).

$$\phi_{j,k}(t)=2^{-j/2}\phi\left(2^{-j}t-k\right) \quad (22a)$$

$$\psi_{j,k}(t)=2^{-j/2}\left(2^{-j}t-k\right) \quad (22b)$$

Where $\phi_{j,k}(t)$ is the scaling function and the function $\psi_{j,k}(t)$ is the wavelets function and * implies the complex conjugate.

The noised SPR signal is decomposed into an approximation and detailed information. In which scaling function $\phi_{j,k}(t)$ is related to the approximate coefficients $a_{j,k}$ and wavelet function is related to the detailed coefficients at level *j*.

Figure 5 the Mallat's cascade algorithm

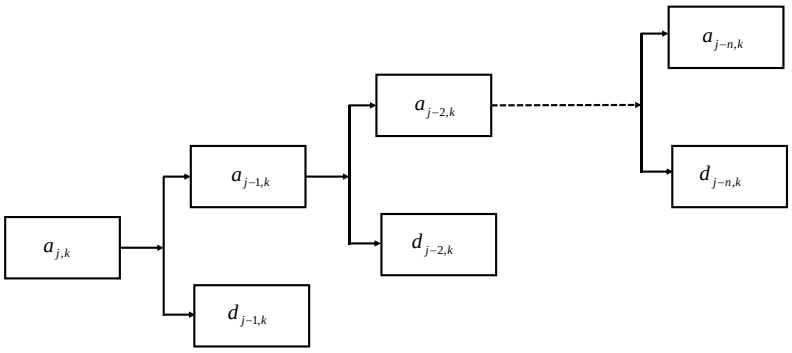

Finally, the filtered signal which is the frequency domain is reconstructed by taking the inverse of DWT (IDWT) to get the spatial filtered SPR signal. The number of levels for both decompositions noised SPR and reconstructed filtered SPR signal are the same.

The coefficients function from different scales can be related by using Mallat's algorithm as follows (Lee & Kim, 2015)

$$a_{j,k}=\sum_{l} h_{l-2k}a_{j+1,j} \quad (23a)$$

$$d_{j,k}=\sum_{l} g_{l-2k}d_{j+1,j} \quad (23b)$$

Where h_k and g_k are low and high pass filters, respectively. In each level, it consists of a low pass filter (LPF) *h(n)* and a high pass filter *g(n)*. The *h(n)* is directly related to the scaling function $\phi_{j,k}(t)$ while *g(n)* is related to the wavelet function $\psi_{j,k}(t)$. A wavelet filter with length L can be mathematically related to *h(n) and g(n)*

$$g(L-1-n)=(-1)^n h(n) \quad (24)$$

Therefore, through the interactive decomposition process, the noised SPR signal is subdivided into lower resolution components meanwhile the noise component is being attenuated. **Figure 5** illustrates the way wavelet filter denoise the signal at different wavelet level.

Algorithm of the denoising SPR signal using wavelet transform

The implementation of the DWT is based on properly selecting the thresholding wavelets coefficient of the noised SPR signal. Here, the

Article DOI: https://doi.org/10.37284/eaje.7.1.2365

energy of the signal with a high noise level is eliminated while the signal with a low noise level will be retained, the process is repeated until the signal with a low noise level is achieved. This process follows three main steps (Lee & Kim, 2015)

a. Decomposition of noised SPR signal into a set of wavelet coefficients. The kind of wavelets used is Symlet wavelets.

b. The selected order was five while the number of levels was varied starting from 1 to 10 until the filtered signal with a high signal-to-noise ratio was obtained.

c. Application of correct thresholding from the resulted wavelets coefficient

d. Reconstruction of the filtered SPR signal into the spatial domain from the reduction of wavelet coefficients

Those three steps can be summarized in the **Figure 6**

Figure 6 Denoising of the SPR signal using wavelet techniques

The thresholding selection

Thresholding is the factor used in wavelets transform to eliminate some coefficient of wavelets transform with high-frequency components from the measure noised SPR signal, the method effectively works for both signal stationary and non-stationary signals (Aggarwal et al., 2011; Lee & Kim, 2015). Thus, the universal threshold value is approximately given by (Aggarwal et al., 2011; Lee & Kim, 2015)

$$Threshold\left(t_{Universal}\right)=\sigma\sqrt{\left(2\log\left(N\right)\right)}$$
$$\sigma=\frac{median\left|\left(Noised\ \ SPR\ coefficient\right)\right|}{0.6745} \quad (25)$$

N is the total number of pixels the CMOS sensor which is 7952 which covers the measurand from air to ethanol without σ is the variance of the noised SPR signal. Normally there are two types of thresholding applied in this research work namely; hard thresholding and soft thresholding. Hard thresholding resets to zero the value of the noised SPR signal or wavelets coefficient less than the threshold $\left(Threshold\left(t_{Universal}\right)\right)$ and sets to logic one for the noised SPR signal or wavelets coefficient greater than the threshold. This kind of thresholding is called gating because it either opens or closes the gates. The hard thresholding $R_h\left(\theta\right)$ can be expressed mathematically as

$$R_h\left(\theta\right)=\begin{cases}R^{'}\left(\theta\right);\ \left|R^{'}\left(\theta\right)\right|>t_{Universal}\\0;\ \left|R^{'}\left(\theta\right)\right|\le t_{Universal}\end{cases} \quad (26)$$

where $R^{'}\left(\theta\right)$ is the noisy SPR reflectance as a function of the angle of the incidence θ.

Soft thresholding sets to zero the noised SPR signal or wavelets coefficient less than the threshold $\left(Threshold\left(t_{Universal}\right)\right)$ and reduces others values to toward zero by decreasing the threshold on the other hand it decreases the noised/roughed effects. The soft thresholding function $R_s\left(\theta\right)$ is given by

$$R_s\left(\theta\right)=\begin{cases}\mathrm{sgn}\left(\left|R^{'}\left(\theta\right)\right|-t_{Universal}\right);\ \left|R\left(\theta\right)\right|>t_{Universal}\\0;\ \left|R^{'}\left(\theta\right)\right|\le t_{Universal}\end{cases} \quad (27)$$

Noise level quantification

Article DOI: https://doi.org/10.37284/eaje.7.1.2365

Table 1 presents the MSE, RMSE, and SNR values for the noisy SPR signal and wavelet-filtered SPR signal. It also demonstrates the variation in the MSE, RMSE, and SNR values when the wavelet filter was applied with different numbers of levels. The noisy SPR signal, extracted from **Figure 3**, represents a signal without the application of the wavelet filter and comprises two sets of air/water and air/ethanol. In this investigation, wavelet filters of Symlet order 5 (sym5) were employed with a number of levels ranging from four to ten, as levels below four produced results that were nearly identical to the unfiltered SPR signal. The values of MSE, RMSE, and SNR were computed based on Equations (11), (12), and (13), respectively. It is noteworthy that lower values of MSE and RMSE correspond to greater SNR for both water and ethanol, which serves as an indicator of the efficacy of the proposed wavelet filter. In the absence of filtration, the SNR was significantly much lower compared to when the wavelet filter was introduced, indicating the filter's capacity to reduce noise levels. The average MSE of water and ethanol as a sample for noised SPR reflectance is 0.011 and reduced to an average of 0.007735 when the wavelets filter was applied at level 8. Similarly, the average RMSE for water and ethanol for noisy SPR signal is 0.1054 decreasing to an average of 0.00815 for water and ethanol. Meanwhile, the average SNR for water and ethanol increased from a noised SPR reflectivity of 18.4241 to 40.1214 dB at level 8. As the number of levels increases up to level 8 the MSE and RMSE are decreased by an average of 30 % and 92.26 %, respectively. However, higher than level 8 the value of MSE and RMSE are decreasing while the SNR is increased by an average of 54.08 %, which implies that the optimum filtering works filter noise when the number of levels is 8 with Symlets with order 5. Notably, at level 8, the MSE and RMSE values reached their minimum, while the SNR attained its maximum. This observation demonstrates that wavelet filters can effectively mitigate noise; however, the optimal number of levels is dependent on the length of the SPR data.

Table 1 MSE, RMSE, and SNR values for noised and filtered SPR signal at different number of levels

Type of the SPR signal	Level	MSE $\times 10^{-04}$		RMSE		SNR (dB)		Standard deviation $\times 10^{-06}$	
		Water	Ethanol	Water	Ethanol	Water	Ethanol	Water	Ethanol
Noised_SPR_signal	noisy	113.00	0.0107	0.1065	0.1042	18.0158	18.8324	1.97	1.97
Filtered_SPR_signal	4	12.000	8.60	0.0356	0.0293	27.9044	29.8435	0.216	0.153
	5	8.0000	4.95	0.0287	0.0223	29.5183	32.2428	0.129	0.0835
	6	6.0100	2.75	0.0237	0.0166	30.7593	34.802	0.103	0.0628
	7	4.1400	1.87	0.0188	0.0137	32.3840	36.477	0.0794	0.0566
	8	96.40	58.3	0.0087	0.0076	38.7091	41.5336	0.0142	0.0222
	9	4.7000	1.87	0.0225	0.0137	31.8254	36.4633	0.0808	0.0444
	10	9.95	5.33	0.0301	0.0231	28.5716	31.9259	0.114	0.156

The **Figure 7** demonstrates the general performance of the wavelet filter at a different number of levels which were produced after estimating the average of MSE, RMSE, SNR, and standard deviation of the noised SPR signal of the values obtained from air/water and air/ethanol set and presented in **Figure (3).** The level zero (0) indicates that no filter was applied to the noised SPR signal. **Figure 7 (a)** shows that the average value of SNR at level 8 is the highest, indicating that Symlet wavelets at order 5 with a data sample of 7952, which is the same as the number of pixels in a CMOS sensor, provide the lowest MSE and RMSE, resulting in higher noise attenuation. Also, shows that the filtered signal is comparable to the theoretical SPR signal.

Article DOI: https://doi.org/10.37284/eaje.7.1.2365

Figure 7 Average value of (a) SNR, (b) MSE (c) RMSE, and (d) standard deviation computed from Table 2

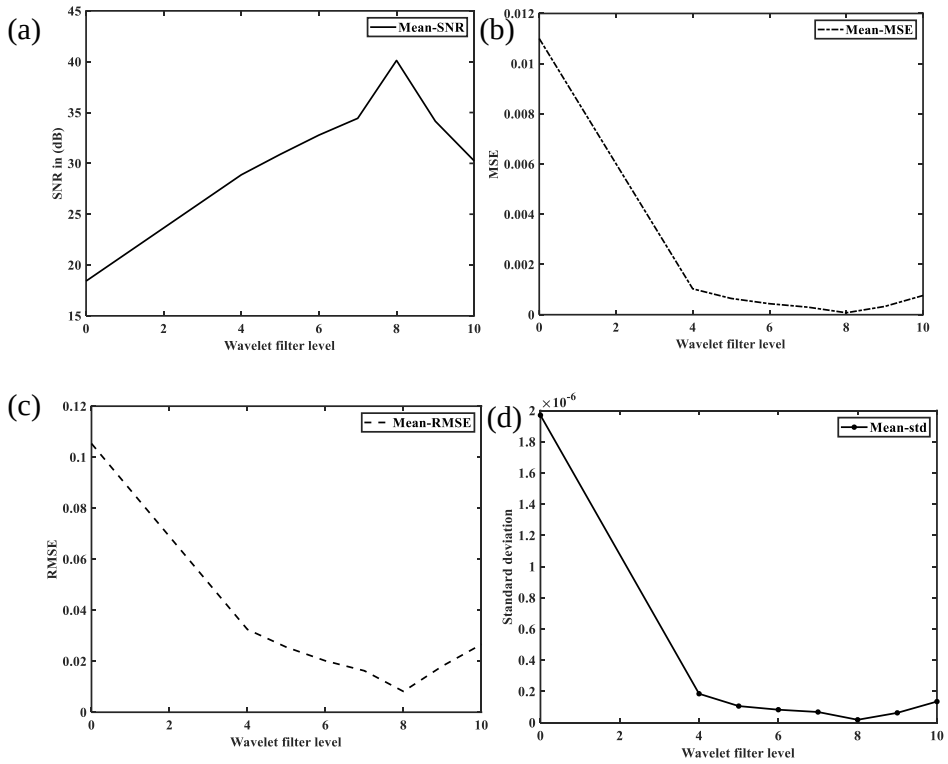

Effect of Wavelets denoising filter to the background noise.

The vertical averaging yields a one-dimensional solution. As can be observed, the recovered SPR reflectivity curve from the P-polarized image contains a lot of noise, which causes it to thicken and shallow. Noise has a negative impact on detection accuracy and resolution of the SPR sensor. The wavelet level was set to 4 since the wavelet filter's effect on lowering background disturbances and blind zone breadth was insignificant at levels 1 through 3. **Figure 8** demonstrates that when the wavelet level increases from 4 to 8, the background noise decreases proportionally. Furthermore, as the wavelet level rises from 4 to 8, the width of the blind zone decreases significantly. The data clearly reveal that level 8 is the best setting for reducing background noise because it produces the average minimal dip. The average value for minimum dip is 0.27, which is shallower than when no filter was usedsamples, and (c) and (d) air and ethanol were utilized.

Figure 8 depicts the impact of wavelet filters at various levels when (a) and (b) air and water were used as

Article DOI: https://doi.org/10.37284/eaje.7.1.2365

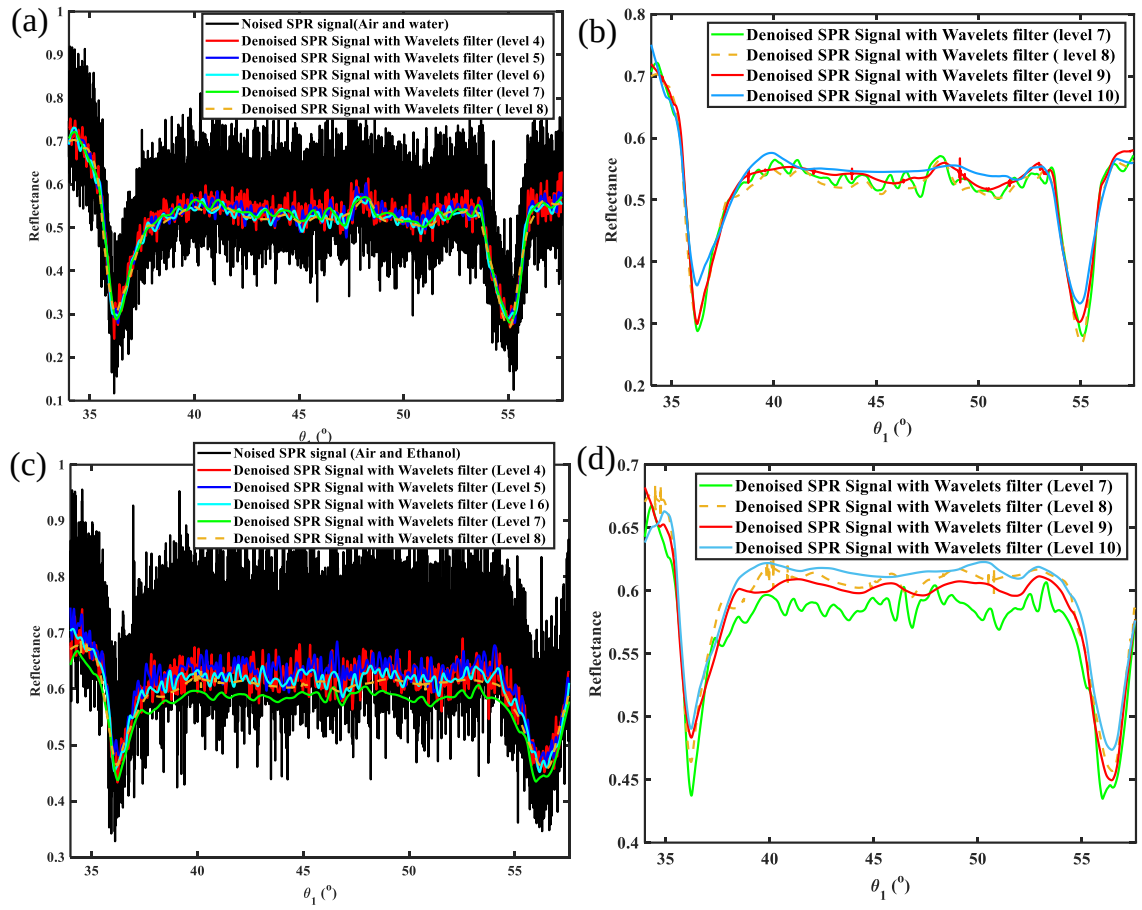

Table 2 demonstrates that the resonance angle results for the theoretical, noisy, and wavelet-filtered SPR data exhibit minimal variation, with an overall error of less than one degree. This observation suggests that the background noise in the SPR sensor had a negligible impact on the resonance position. However, the adverse effects of noise hinder the detection of the minimum dip and impede the resolution of slight changes in the refractive index, consequently leading to diminished resolution.

Table 2 Background noise effect on resonance angle of the SPR data in comparison to theoretical and wavelet filter

Samples	Resonance angle (˚)				
	Theoretical	***Without filter***	***Error***	***With Wavelet filter***	***Error***
Air	36.1000	36.3945	0.2945	36.4225	0.3225
Water	54.6000	55.1081	0.5081	55.0547	0.4547
Ethanol	56.2400	56.2530	0.013	56.3012	0.0612
Average Resonance angle error			0.2719		0.2795

Table 3 demonstrates that the full width at half maximum (FWHM) for the theoretical surface plasmon resonance (SPR) exhibits the broadest FWHM compared to the noisy and wavelet-filtered SPR data. However, the filtered SPR data present a narrower FWHM than the theoretical SPR sensor due to the corruption of the ideal signal by background noise; consequently, when filtering is applied to a corrupted signal, the influence of noise is the primary factor

Article DOI: https://doi.org/10.37284/eaje.7.1.2365

contributing to the narrower-than-theoretical FWHM. The results indicate that when corrupted SPR data are subjected to the proposed wavelet filter, the FWHM can be enhanced, leading to improved detection accuracy, and the SPR spectrum appears narrower than the noisy counterpart. This observation suggests that background noise in the SPR sensor significantly affects the FWHM. The wavelet filter demonstrated an average improvement in FWHM of 47.27%. The curve characteristics, including its shape, full width at half maximum (FWHM), and position of the SPR dip, are of considerable importance for sensing applications. A smaller FWHM value corresponds to a narrower curve, indicating enhanced measurement accuracy.

Table 3: Effect of background noise on FWHM of SPR data in comparison to theoretical and wavelet Filter Results

Samples	FWHM (°)				
	Theoretical	***Without filter***	***Error***	***With Wavelets filter***	***Error***
Air	1.3900	1.9456	0.5556	1.3231	0.0669
Water	3.3300	2.0950	-1.2350	1.5563	-1.7737
Ethanol	3.3800	2.3282	-1.0518	1.7283	-1.6517
Average FWHM	2.7	2.1229	-0.5771	1.5359	-1.1195

From **Table 4**, it is observed that the theoretical SPR exhibits the most pronounced minimum dip in comparison to the noised and wavelet-filtered SPR data. Conversely, the noised SPR data demonstrates the shallowest minimum dip due to the influence of background noise. It is noted that the proposed wavelet filtering method can enhance the average minimum dip by 41.22%. The presence of a shallow minimum dip necessitates the implementation of a complex detection algorithm to accurately determine the resonance position.

Table 4; **Background noise effect on minimum dip in comparison to theoretical and wavelet filter of the SPR data**

Samples	Minimum Dip (A.U)				
	Theoretical	***Without filter***	***Error***	***With Wavelet filter***	***Error***
Air	0.0074	0.6543	0.6469	0.3803	0.3729
Water	2.8975×10^{-5}	0.6342	0.6342	0.2934	0.2933
Ethanol	0.0002	0.6342	0.6340	0.4565	0.4563
Average minimum dip	0.0038	0.6409	0.6384	0.3767	0.3742

Measurement parameters of the SPR sensor

As demonstrated in **Table 5**, the sensitivity to RI change of the designed biosensor is approximately equivalent to that without the application of the wavelet filter. As previously noted, the background noise primarily affects the shape of SPR reflectivity by broadening it, resulting in a shallower dip. However, the detection accuracy of the designed SPR sensor with the application of the wavelet filter is improved by 27.56% compared to that without the application of the filter (DA = 9.4002/°), as a consequence of narrower FWHM, given that the detection accuracy is inversely proportional to the FWHM. Conversely, the noised SPR signal yields a higher detection accuracy compared to the theoretical value, which is erroneous; the higher values suggest false detection resulting from the broadening of the SPR reflectivity curve, as illustrated in **Figure 7.**

The sensor merit (SM) of the theoretical SPR is the highest compared to the noisy and filtered SPR data, which is caused by the deepest minimum dip which implies the transformation of photon energy to plasmon energy is stronger and the SPR signal is not corrupted by background noise. Meanwhile, in noisy SPR the reflectivity is shallow because the SPR is corrupted by the

Article DOI: https://doi.org/10.37284/eaje.7.1.2365

background noise. However, the proposed wavelets filter shows how effective is by improving SM in the percentage of 42 % in comparison with noised SPR data. A similar trend follows the CSF, in which theoretical SPR has a higher value compared to noisy and wavelet-filtered SPR the reason is similar to SM because is proportional to SM and sensitivity. CSF was improved by 41.94 % which is almost the same as SM. As stated earlier the sensitivity for all cases is almost the same.

Furthermore, the impact of noise is evident in the resolution, as the noised SPR signal has decreased by 98.54 % compared to the ideal SPR reflectivity (3.7523×10^{-6}) (see **Table 5**). From **Table 5**, the proposed wavelet filter enhances the resolution by reducing it from 2.567×10^{-4} to 1.3772×10^{-7}, which is significantly enhanced by 99.95% from corrupted SPR signal with noisy. Despite the SPR sensor having a wide dynamic range it gives a resolution much higher than what was reported (Jiří Homola, Yee, & Gauglitz, 1999; Ma et al., 2019; Widjaja & Hossea, 2021). Additionally, the results validate the efficacy of the proposed wavelet filter in noise removal and improvement of SPR sensor performance. Moreover, it is evident that the proposed wavelet filter applied to the SPR sensor provides a substantially higher FOM compared to previously published SPR sensors that did not employ the filter (Didar & Vahed, 2023; Dostálek, Homola, & Miler, 2005; Lin & Chen, 2019).

Table 5 The performance of the SPR sensor reflectivity data based on wavelet filter

	S (deg/RIU)	DA (1/deg)	FOM (1/RIU)	SM (1/deg)	CSF(1/RIU)	Resolution (RIU)
Theoretical SPR	56.2295	7.4140	20.8258	0.2579	14.4989	3.7523×10^{-6}
SPR without filter	56.055	9.4002	26.4051	0.1221	06.8415	2.567×10^{-4}
SPR with filter	55.9822	12.9759	36.4491	0.2105	11.7840	1.3772×10^{-7}

Conclusion

The study's findings show that integrating wavelet filtering techniques significantly boosts the performance of divergence beam-based SPR sensors. Significant improvements were achieved in a number of important metrics with the advanced wavelet-based approach. Specifically, there was a 30 % reduction in the mean square error (MSE) and a 92.26 %, reduction in the root mean square error (RMSE), indicating improved signal accuracy. An improvement of 54.08 %, was observed in the signal-to-noise ratio (SNR), indicating better signal clarity and noise reduction. The combined sensitivity factor (CSF) demonstrated a striking increase of 41.94 %, highlighting the overall improvement in sensor precision and robustness. In addition, the sensitivity matrix (SM) increased by 42 %, reflecting increased sensor responsiveness. These enhancements are ascribed to the wavelet filter's capacity for multi-resolution signal decomposition, which permits efficient noise isolation and attenuation across various frequency bands while preserving crucial signal properties. As a result, the sensor's operating efficiency is maximized and refractive index detection and resolution are improved by 99.95 % from noisy SPR data. These metrics' performance improvements validate that the wavelet filter can outperform conventional filtering methods and offer a potent tool for improving the capabilities of diverging beam-based SPR sensors in environment and biosensing applications.

Acknowledgement

The author would like to thank the Dar es Salaam Institute of Technology (DIT) for supporting this study.

REFERENCES

Aggarwal, R., Singh, J. K., Gupta, V. K., Rathore, S., Tiwari, M., & Khare, A. (2011). Noise reduction of speech signal using wavelet transform with modified universal threshold. *International Journal of Computer Applications*, *20*(5), 14-19.

Article DOI: https://doi.org/10.37284/eaje.7.1.2365

Bahrami, F., Alam, M., Aitchison, J., & Mojahedi, M. (2013). Dual polarization measurements in the hybrid plasmonic biosensors. *Plasmonics, 8*, 465-473.

Balan, S., Khaparde, A., Tank, V., Rade, T., & Takalkar, K. (2014). *Under water noise reduction using wavelet and savitzky-golay*. Paper presented at the Second international conference on computational science and engineering.

Boecker, D., Zybin, A., Niemax, K., Grunwald, C., & Mirsky, V. M. (2008). Noise reduction by multiple referencing in surface plasmon resonance imaging. *Review of scientific instruments, 79*(2).

Boruah, R., Mohanta, D., Choudhury, A., Nath, P., & Ahmed, G. A. (2015). Surface plasmon resonance-based protein bio-sensing using a Kretschmann configured double prism arrangement. *IEEE Sensors Journal, 15*(12), 6791-6796.

Ceballos-Zumaya, J., Sustaita-Torres, I., Pérez-Huerta, J., Ariza-Flores, D., & Madrigal-Melchor, J. (2024). Performance parameters as a function of graphene's chemical potential for SPR biosensor based on 2D materials. *Optik*, 172013.

Chan, B. L., & Jutamulia, S. (2012). *SPR prism sensor using laser line generator*. Paper presented at the Plasmonics in Biology and Medicine IX.

Chen, R., Wang, M., Wang, S., Liang, H., Hu, X., Sun, X., Hu, J. (2015). A low-cost surface plasmon resonance biosensor using a laser line generator. *Optics Communications, 349*, 83-88.

Chinowsky, T., Quinn, J., Bartholomew, D., Kaiser, R., & Elkind, J.(2003). Performance of the Spreeta 2000 integrated surface plasmon resonance affinity sensor. *Sensors and Actuators B: Chemical, 91*(1-3), 266-274.

Dai, J., & Fu, L.-h. (2024). Denoising of Surface Plasmon Resonance (SPR) Spectra Using the Generalized S-transform and the Bald Eagle Search (BES) Algorithm. *Analytical Letters, 57*(11), 1778-1788.

de Aguiar, G. M., Souza, L. C., de Souza, D. F., & Oliveira, L. C. (2022). Combination of digital image processing and statistical data segmentation to enhance SPR and SPRi sensor responses. *Plasmonics, 17*(3), 1033-1039.

Didar, R. F., & Vahed, H. (2023). Improving the performance of high-sensitivity surface plasmon resonance biosensor with 2D nanomaterial coating (BP-WS2) based on hybrid structure: Theoretical analysis. *IET Optoelectronics, 17*(6), 284-293.

Dostálek, J., Homola, J., & Miler, M. (2005). Rich information format surface plasmon resonance biosensor based on array of diffraction gratings. *Sensors and Actuators B: Chemical, 107*(1), 154-161.

Goodman, J. W. (2007). *Speckle phenomena in optics: theory and applications*: Roberts and Company Publishers.

Hickel, W., & Knoll, W. (1991). Time-and spatially resolved surface plasmon optical investigation of the photodesorption of Langmuir-Blodgett multilayer assemblies. *Thin Solid Films, 199*(2), 367-373.

Homola, J. (2008). Surface plasmon resonance sensors for detection of chemical and biological species. *Chemical reviews, 108*(2), 462-493.

Homola, J., Yee, S. S., & Gauglitz, G. (1999). Surface plasmon resonance sensors. *Sensors and Actuators B: Chemical, 54*(1-2), 3-15.

Hossea, J., & WidJaJa, J. (2020). Effects of Prism Types and Materials on Divergent Beam Illumination and Detection in Surface Plasmon Resonance (SPR) Sensors. *International*

Journal of Laser Science: Fundamental Theory & Analytical Methods, 2(1).

Article DOI: https://doi.org/10.37284/eaje.7.1.2365

Hossea, J. H., & Rugumira, G. (2024). Analytical Design of a Portable Surface Plasmon Resonance Sensor by Using a Divergence Beam for Measuring Multiple Heavy Metals and Other Contamination Simultaneously. *East African Journal of Engineering, 7*(1), 148-161.

Hossea, J. H., & Widjaja, J. (2017). *Design of surface plasmon resonance biosensors by using powell lens.* Paper presented at the 2017 International Electrical Engineering Congress (iEECON).

Hu, J., Cao, B., Wang, S., Li, J., Wei, W., Zhao, Y., . . . Sun, X. (2016). Design and fabrication of an angle-scanning based platform for the construction of surface plasmon resonance biosensor. *Optics and Lasers in Engineering, 78*, 1-7.

Huang, Y., Zhang, L., Zhang, H., Li, Y., Liu, L., Chen, Y., . . . Yu, D. (2020). Development of a portable SPR sensor for nucleic acid detection. *Micromachines, 11*(5), 526.

Isaacs, S., & Abdulhalim, I. (2015). Long range surface plasmon resonance with ultra-high penetration depth for self-referenced sensing and ultra-low detection limit using diverging beam approach. *Applied physics letters, 106*(19).

Karabchevsky, A., Karabchevsky, S., & Abdulhalim, I. (2011). Fast surface plasmon resonance imaging sensor using Radon transform. *Sensors and Actuators B: Chemical, 155*(1), 361-365.

Kretschmann, E. (1971). The determination of the optical constants of metals by excitation of surface plasmons. *Zeitschrift für Physik A Hadrons and nuclei, 241*, 313-324.

Kretschmann, E., & Raether, H. (1968). Radiative decay of nonradiative surface plasmons excited by light. *Zeitschrift für Naturforschung A, 23*(12), 2135-2136.

Lee, S., & Kim, J. (2015). Discrete wavelet transform-based denoising technique for advanced state-of-charge estimator of a lithium-ion battery in electric vehicles. *Energy, 83*, 462-473.

Lenferink, A. T., Kooyman, R., & Greve, J. (1991). An improved optical method for surface plasmon resonance experiments. *Sensors and Actuators B: Chemical, 3*(4), 261-265.

Lin, C., & Chen, S. (2019). Design of high-performance Au-Ag-dielectric-graphene based surface plasmon resonance biosensors using genetic algorithm. *Journal of Applied Physics, 125*(11).

Ma, K., Liu, L., Zhang, P., He, Y., & Peng, Q. (2019). Optimization of angle-pixel resolution for angular plasmonic biosensors. *Sensors and Actuators B: Chemical, 283*, 188-197.

Mohanty, B. C., & Kasiviswanathan, S. (2005). Two-prism setup for surface plasmon resonance studies. *Review of scientific instruments, 76*(3).

Moreira, C., Lima, A., Neff, H., & Thirstrup, C. (2008). Temperature-dependent sensitivity of surface plasmon resonance sensors at the gold–water interface. *Sensors and Actuators B: Chemical, 134*(2), 854-862.

Ohkita, H., Abe, Y., Kojima, H., Tagaya, A., & Koike, Y. (2004). Birefringence reduction method for optical polymers by the orientation-inhibition effect of silica particles. *Applied physics letters, 84*(18), 3534-3536.

Oliveira, L. C., Lima, A. M. N., Thirstrup, C., & Neff, H. F. (2019). *Surface plasmon resonance sensors: a materials guide to design, characterization, optimization, and usage* (Vol. 70): Springer.

Otto, A. (1968). Excitation of nonradiative surface plasma waves in silver by the method of frustrated total reflection. *Zeitschrift für Physik A Hadrons and nuclei, 216*(4), 398-410.

Article DOI: https://doi.org/10.37284/eaje.7.1.2365

Patskovsky, S., Meunier, M., Prasad, P. N., & Kabashin, A. V. (2010). Self-noise-filtering phase-sensitive surface plasmon resonance biosensing. *Optics express, 18*(14), 14353-14358.

Pavlov, I., Vedyashkina, A., & Yanina, G. (2019). *The choice of an image processing algorithm for increasing sensitivity of the surface plasmon resonance method.* Paper presented at the Journal of Physics: Conference Series.

Pluchery, O., Vayron, R., & Van, K.-M. (2011). Laboratory experiments for exploring the surface plasmon resonance. *European journal of physics, 32*(2), 585.

Sharma, A. K., & Dominic, A. (2017). Influence of chemical potential on graphene-based SPR sensor's performance. *IEEE Photonics Technology Letters, 30*(1), 95-98.

Vlcek, J., Pistora, J., & Lesnák, M. (2009). *Sensitivity enhancement in surface plasmon resonance sensors: theoretical modeling.* Paper presented at the Optical Sensors 2009.

Wang, G., Wang, K., Ren, J., Ma, S., & Li, Z. (2022). A novel doublet-based surface plasmon resonance biosensor via a digital Gaussian filter method. *Sensors and Actuators B: Chemical, 360*, 131680.

Wang, T., Zhang, C., Aleksov, A., Salama, I., & Kar, A. (2016). Effect of large deflection angle on the laser intensity profile produced by acousto-optic deflector scanners in high precision manufacturing. *Journal of Laser Applications, 28*(1).

Widjaja, J., & Hossea, J. (2021). Experimental Validations of Divergent Beam Illumination and Detection Conditions in a Surface Plasmon Resonance Sensor Using a Powell Lens. *Lasers in Engineering (Old City Publishing), 48*.

Yamamoto, M. (2002). Surface plasmon resonance (SPR) theory: tutorial. *Review of Polarography, 48*(3), 209-237.

